

# RIS-enabled Multi-user $M$ -QAM Uplink NOMA Systems: Design, Analysis, and Optimization

Mahmoud AlaaEldin, *Member, IEEE*, Mohammad Al-Jarrah, *Member, IEEE*, Xidong Mu, *Member, IEEE*, Emad Alsusa, *Senior Member, IEEE*, Karim G. Seddik, *Senior Member, IEEE*, and Michail Matthaiou, *Fellow, IEEE*

**Abstract**—Non-orthogonal multiple access (NOMA) is widely recognized for enhancing the energy and spectral efficiency through effective radio resource sharing. However, uplink NOMA systems face greater challenges than their downlink counterparts, as their bit error rate (BER) performance is hindered by an inherent error floor due to error propagation caused by imperfect successive interference cancellation (SIC). This paper investigates BER performance improvements enabled by reconfigurable intelligent surfaces (RISs) in multi-user uplink NOMA transmission. Specifically, we propose a novel RIS-assisted uplink NOMA design, where the RIS phase shifts are optimized to enhance the received signal amplitudes while mitigating the phase rotations induced by the channel. To achieve this, we first develop an accurate channel model for the effective user channels, which facilitates our BER analysis. We then introduce a channel alignment scheme for a two-user scenario, enabling efficient SIC-based detection and deriving closed-form BER expressions. We further extend the analysis to a generalized setup with an arbitrary number of users and modulation orders for quadrature amplitude modulation signaling. Using the derived BER expressions, we develop an optimized uplink NOMA power allocation (PA) scheme that minimizes the average BER while satisfying the user transmit power constraints. It will be shown that the proposed NOMA detection scheme, in conjunction with the optimized PA strategy, eliminate SIC error floors at the base station. The theoretical BER expressions are validated using simulations, which confirms the effectiveness of the proposed design in eliminating BER floors.

**Index Terms**—Bit error rate, power allocation, reconfigurable intelligent surfaces, uplink NOMA.

In recent years, there has been an unprecedented increase in the number of mobile terminals, Internet of Things (IoT) devices, and autonomous vehicles, placing a tremendous burden on the existing limited radio resources. Moreover, emerging technologies, such as holographic communications, virtual and augmented reality applications, video streaming, and online gaming, all of which require massive data rates, have further amplified the demand for efficient utilization of these resources. To address this challenge, non-orthogonal multiple access (NOMA) has been proposed as a revolutionary multiple-access technique that can in theory enhance the spectral efficiency. As a result, NOMA has gained significant attention from both academia and industry

and is regarded a key candidate for future sixth-generation (6G) networks and beyond [1]–[3]. NOMA is categorized into two main schemes: power-domain NOMA and code-domain NOMA. In the former, users are assigned different power levels based on their channel conditions to the base station (BS), while in the latter, each user is assigned a unique code as a signature. This paper focuses on power-domain NOMA, where multiple devices share the same time-frequency resource block with different power levels, and successive interference cancellation (SIC) is employed at the receiver to effectively decode the signals [4].

Likewise, reconfigurable intelligent surfaces (RISs) have emerged in recent years as smart technology capable of improving the quality of wireless communication links [5]–[9]. An RIS typically consists of a large number of low-cost, tunable passive elements that can adjust the amplitudes and phase shifts of incident waves, effectively reflecting or refracting them toward the receiver. The key advantage of RISs lies in their ability to customize the wireless channel to support various critical features, such as signal enhancement and interference mitigation. Consequently, the integration of RISs into diverse wireless systems has been extensively studied in recent literature. For example, in [10], the authors developed alternation minimization algorithms to minimize the total transmit power by jointly optimizing the active beamforming at the BS and the passive beamforming at the RIS. In [11], the maximization of the energy efficiency (EE) of RIS-assisted downlink systems was considered. Furthermore, a joint power and user association scheme for a multi-RIS-assisted multi-BS system using millimeter waves was proposed in [12].

## A. Related work

Since NOMA is capable of approaching the boundary of the capacity region, multiple works in the literature have studied the integration of NOMA in RIS-enabled systems as a win-win solution [13], [14]. In the following, we provide a review of the literature focusing on the performance analysis of uplink RIS-NOMA systems.

The authors of [15] studied the outage performance of a simplified RIS enabled uplink two-user NOMA system. Specifically, they derived approximate analytical expressions for the received powers of the NOMA users as Gamma random variables (RVs) using the method of moment matching, which resulted in tractable expressions of the outage probability with SIC. In addition, the study in [16] analyzed the outage performance of a RIS-assisted two-user uplink NOMA system, which divided the RIS elements into

Mahmoud AlaaEldin, Xidong Mu, and Michail Matthaiou are with the Centre for Wireless Innovation (CWI), Queen's University Belfast, Belfast BT3 9DT, UK (e-mail: m.alaeldin@qub.ac.uk; x.mu@qub.ac.uk; m.matthaiou@qub.ac.uk)

Mohammad Al-Jarrah and Emad Alsusa are with the Electrical and Electronic Engineering Department, University of Manchester, Manchester M13 9PL, UK (e-mail: mohammad.al-jarrah@manchester.ac.uk; e.alsusa@manchester.ac.uk).

Karim G. Seddik is with the Department of Electronics and Communications Engineering, American University in Cairo, Cairo, Egypt 11835 (e-mail: kseddik@aucegypt.edu).

	Our work	[15]	[16]	[17]	[18]	[19]
RIS-NOMA	✓	✓	✓	✓	✓	✓
Uplink	✓	✓	✓	✓	✓	✓
BER analysis	✓	✗	✗	✗	✗	✗
Arbitrary # of users	✓	✗	✗	✗	✗	✗
Arbitrary Mod. orders	✓	✗	✗	✗	✗	✗
BER based uplink PA	✓	✗	✗	✗	✗	✗

Table I: Distinguishing the work in this paper from other existing works in the literature

two groups to improve each user's signal. By approximating the received powers as Gamma RVs, they derived outage probability expressions for uplink NOMA signaling using SIC. The authors of [17] investigated downlink and uplink RIS-aided NOMA and orthogonal multiple access (OMA) systems, where an RIS is applied to enhance the coverage for a cell-edge user communicating with the BS. Closed-form expressions for the outage probability and ergodic rate under Nakagami- $m$  fading have been derived. Using asymptotic approximations in the high signal-to-noise-ratio (SNR) regime, it has been revealed that there is a diversity order that depends on the number of RIS elements and fading parameters, while the high SNR slope is unaffected. In [18], the authors studied the symbol error rate (SER) performance of simultaneously transmitting and reflecting reconfigurable intelligent surface (STAR-RIS) aided uplink NOMA, where the phase shift and amplitude parameters were adjusted based on distance-maximizing constellation scaling and rotation to enhance the SER performance of the system. However, closed-form SER expressions were not derived in [18] as the expressions are given by  $K$ -fold integrals. Finally, the authors of [19] investigated the ergodic sum-rate of the STAR-RIS assisted uplink NOMA under channel estimation errors and hardware impairments, where upper bounds were derived for perfect and imperfect SIC-based decoding.

### B. Motivations and Contributions

From the literature review, it is evident that most of the existing works have focused on the analysis of the achievable rate and outage capacity of RIS-enabled uplink NOMA systems. To the best of the authors' knowledge, the investigation of reliability metrics, such as bit error rate (BER), has not been considered in the literature. Studying the BER performance analysis is indispensable for characterizing the reliability of communication systems, as it helps to predict the error rate of the received data, which has a direct impact on the effective throughput of communication links. Therefore, to bridge this clear gap in the literature, this paper provides a comprehensive study of the BER performance limits of uplink RIS-NOMA systems under imperfect SIC. Similar to existing literature [15], [16], [19], [20], the RIS is partitioned into  $K$  partitions, where  $K$  is the number of users, and each partition is assigned to a certain user. Then, the phase shifts of each RIS partition are adjusted to maximize the effective channel of the corresponding user. This partitioning technique allows us to statistically model the effective channels of the users which is required to derive the average BER analytical expressions.

The key contributions of this work are summarized as follows:

- A detailed and accurate statistical modeling of the effective channels of the users is introduced based on dividing the RIS panel into  $K$  partitions and assigning each partition to a certain user.
- A novel channel alignment scheme is then devised to align the effective channels of the users on the real axis to eliminate the relative phase shifts between the effective channels of the users. This allows for the construction of a simple and tractable SIC-based detection of the users' symbols at the BS. The proposed channel alignment facilitates the BER performance analysis of the two-user uplink RIS-NOMA scenario.
- An extension of the BER analysis is conducted for the case of arbitrary number of users and quadrature amplitude modulation (QAM) modulation orders, providing valuable insights on the achievable performance of the RIS-NOMA system. This is done by devising an algorithm that computes the coefficients of the BER expressions for any system with arbitrary parameters.
- A power allocation (PA) scheme that utilizes the derived BER expressions is devised to eliminate the BER floors, by minimizing the average BER of all users subject to individual uplink transmit power constraints for the users.
- Simulation results verify the accuracy and effectiveness of the proposed closed-form generic analytical BER expressions. The results also reveal the efficacy of the proposed PA scheme, showing that it completely eliminates the BER floors. Moreover, we compare RIS-NOMA systems with the equivalent RIS-OMA counterparts. The results confirm the superiority of RIS-NOMA over RIS-OMA across all scenarios and almost all SNR values when both systems maintain the same channel estimation overhead for a fair comparison. However, if the additional channel estimation, computational demands, and hardware complexities of RIS-OMA are ignored, it may slightly outperform RIS-NOMA in cases with low modulation orders and a limited number of reflectors. Nonetheless, this comparison would not be fair.

Finally, Table I explicitly contrasts our contributions to the existing works on RIS-NOMA in the literature.

### C. Organization and Notations

The rest of the paper is organized as follows: In Sec. I, the RIS-enabled uplink NOMA system model is presented. The statistical modeling and channel alignment of the RIS uplink channels is presented in Sec. II. In Sec. III, we present the BER analysis of the two-user uplink RIS-NOMA system, whereas the analysis is extended in Sec. IV for the generalized system with an arbitrary number of NOMA users and arbitrary modulation orders. An optimized uplink PA scheme for the uplink RIS-NOMA system is discussed in Sec. V. The simulation results and discussion are given in Sec. VI, while the conclusions of this work are presented in Sec. VII.

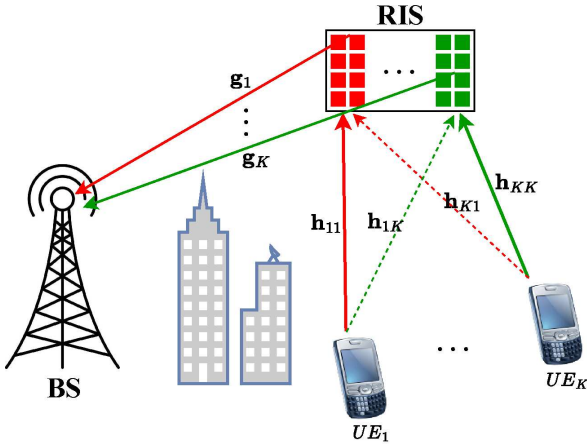


Figure 1: RIS-enabled uplink NOMA system model

*Notations:* The bold lowercase letters are used to define vectors, while the bold uppercase letters are used to define matrices. The  $|\cdot|$ ,  $\Re(\cdot)$ ,  $\Im(\cdot)$ ,  $\arg(\cdot)$ , and  $(\cdot)^*$  are the absolute, real, imaginary, angle, and conjugate of a complex number, while  $j' = \sqrt{-1}$  is the imaginary number.

## I. SYSTEM MODEL

As shown in Fig. 1, we consider an uplink RIS-enabled NOMA system that contains a single antenna BS, an RIS with  $L$  reflectors, and  $K$  single antenna users, where the  $i$ th user is denoted by  $U_i$ . In our proposed design, we assume that the RIS is divided into separate  $K$  partitions, denoted as  $\mathcal{P}_1, \mathcal{P}_2, \dots, \mathcal{P}_K$ , where partition  $\mathcal{P}_i$  is assigned to  $U_i$  and contains  $L_i$  reflection elements of the RIS, i.e.,  $\sum_{k=1}^K L_k = L$ . The RIS phase shifts of each partition are adjusted to align the channels of the corresponding user so that the received signal components of each user are coherently added at the destination. As shown in Fig. 1, the channel vector from  $U_i$  to its associated RIS partition,  $\mathcal{P}_i$ , is denoted as  $\mathbf{h}_{ii} \in \mathbb{C}^{L_i \times 1}$ . On the other hand, the cross channel vector from  $U_i$  to the partition  $\mathcal{P}_j$  is denoted as  $\mathbf{h}_{ij} \in \mathbb{C}^{L_j \times 1}$ . Moreover, the channel vector from the  $i$ th portion,  $\mathcal{P}_i$ , to the BS is denoted as  $\mathbf{g}_i \in \mathbb{C}^{L_i \times 1}$ . Therefore, the received superimposed NOMA signal,  $y$ , at the BS can be expressed as

$$y = \sum_{i=1}^K \sum_{j=1}^K \sqrt{\frac{P_i \eta_i}{\beta_i}} \mathbf{h}_{ij}^T \Theta_j \mathbf{g}_j x_i + n, \quad (1)$$

where  $P_i$  denotes the transmit power of  $U_i$ ,  $\eta_i$  represents the overall path loss of the cascaded channel, i.e., user-RIS-BS link, and  $\Theta_j$  is a diagonal matrix whose diagonal elements are the  $\mathcal{P}_j$  reflection coefficients, i.e.,  $\Theta_j = \text{diag}\{e^{j'\theta_{j,1}}, e^{j'\theta_{j,2}}, \dots, e^{j'\theta_{j,L_j}}\}$ , with  $\theta_{j,l}$  representing the phase shift introduced by the  $l$ th reflecting element of  $\mathcal{P}_j$ . The term  $x_i \in \mathbb{C}$  denotes the transmitted modulation symbol of  $U_i$ , drawn from a square QAM alphabet,  $\mathcal{X}_i$ , where the cardinality of  $\mathcal{X}_i$  is the QAM modulation order of  $U_i$ . Since the data symbols,  $x_i$ , are drawn from square QAM constellations, both the real and imaginary components of  $x_i$  can take values from the set  $\{\pm 1, \pm 3, \dots, \pm \sqrt{M_i} - 1\}$ , where  $M_i$  is the modulation

order of  $U_i$ . The scaling factor,  $\beta_i \triangleq \frac{2}{3}(M_i - 1)$ , is used to normalize  $x_i$  to unity. The parameter,  $\eta_i = \eta_{U_i, I} \eta_{I, B}$ , in (1) is the overall path loss of the  $U_i$ -RIS-BS link, where  $\eta_{U_i, I} = d_{U_i, I}^{-\psi}$ ,  $\eta_{I, B} = d_{I, B}^{-\psi}$ ;  $d_{U_i, I}$  is the distance between the  $i$ th user and RIS,  $d_{I, B}$  is the BS-RIS distance, where  $\psi$  is the path loss exponent of the wireless links. The additive white Gaussian noise at BS is denoted by  $n$ , and it is modeled as a complex Gaussian RV with zero mean and variance of  $\sigma_n^2$  per complex dimension, i.e.,  $n \sim \mathcal{CN}(0, 2\sigma_n^2)$ .

The channel vectors  $\mathbf{g}_j$  and  $\mathbf{h}_{ij}, \forall i, j$  are assumed to be Rayleigh fading channels. Therefore, the elements of  $\mathbf{h}_{ij}$  and  $\mathbf{g}_j$  are assumed as independent and identically distributed (i.i.d.) complex normal RVs with zero mean and unit variance, i.e.,  $\mathbf{h}_{ij}, \mathbf{g}_j \sim \mathcal{CN}(\mathbf{0}, \mathbf{I})$ . The RIS is assumed to have full knowledge of the phases of  $\mathbf{h}_{ii}$  and  $\mathbf{g}_i, \forall i$ , so that the phase shifts of the RIS reflection elements can be adjusted to reflect incident signals with concentrated beams towards the BS. It should be noted that there is no need for the estimation of the channels of all RIS elements to the users, i.e., knowledge of the cross channel vectors,  $\mathbf{h}_{i,j}, \forall i \neq j$ , is not required. Since the  $i$ th user,  $U_i$ , is assigned a separate partition of the RIS,  $\mathcal{P}_i$ , the phase shifts of  $\mathcal{P}_i$  are adjusted to maximize the reflected signal from  $\mathcal{P}_i$  at the BS. However,  $U_i$  signal reflections from other RIS partitions,  $\mathcal{P}_j, \forall j \neq i$ , are considered random signal reflections, since the phase shifts of these partitions are not adjusted to the  $U_i$  channels. Therefore, two signal components of  $U_i$  are received at the BS, namely, the optimized component and the random component. To maximize the reflected signal component of  $\mathcal{P}_i$  received at the BS, the adjustable phase shifts of  $\mathcal{P}_i$  are set as  $\theta_{i,l} = -(\arg(h_{ii,l}) + \arg(g_{i,l})), \forall l = 1, \dots, L_i$ , where  $\theta_{i,l}$  is the phase shift of the  $l$ th reflection element of  $\mathcal{P}_i$ , and  $h_{ii,l}$  and  $g_{i,l}$  are the  $l$ th elements of  $\mathbf{h}_{ii}$  and  $\mathbf{g}_i$ , respectively. As a result, the total received superimposed signal at the BS can be written as

$$y = \sum_{i=1}^K \left( \gamma_{ii} + \sum_{j=1, j \neq i}^K \gamma_{ij} \right) x_i + n, \quad (2)$$

where  $\gamma_{ii}$  is the optimized component of the RIS effective channel of the  $i$ th user, reflected from its allocated partition,  $\mathcal{P}_i$ , which can be expressed as

$$\gamma_{ii} = \sqrt{\frac{P_i \eta_i}{\beta_i}} \sum_{l=1}^{L_i} |h_{ii,l}| |g_{i,l}|. \quad (3)$$

The terms,  $\gamma_{ij}, \forall j \neq i$ , are the random components of the RIS effective channel of user  $i$ , reflected from the other users' partitions,  $\mathcal{P}_j, \forall j \neq i$ , which can be expressed as

$$\gamma_{ij} = \sqrt{\frac{P_i \eta_i}{\beta_i}} \sum_{l=1}^{L_j} h_{ij,l} e^{j'\theta_{j,l}} g_{j,l}, \quad (4)$$

where  $h_{ij,l}$  is the  $l$ th element of  $\mathbf{h}_{ij}$ , and  $g_{j,l}$  is the  $l$ th element of  $\mathbf{g}_j$ .

In the next section, we provide an accurate statistical modeling for the RIS effective channels and a channel alignment scheme to align the effective channels of the users. This will

be used to derive closed-form average BER expressions in the subsequent sections.

## II. STATISTICAL MODELING AND ALIGNMENT OF THE RIS EFFECTIVE CHANNELS OF THE USERS

In this section, accurate statistical modeling is derived for both the optimized component,  $\gamma_{ii}$ , and the random components,  $\gamma_{ij}$ , of the RIS effective channel of the  $i$ th user. Moreover, a channel alignment scheme is devised to align the effective channels of the users to the zero axis, which later facilitates simple detection and the BER derivations. The statistical models of the channel components derived in this section will be used in Sec. III and Sec. IV for the calculation of the unconditional average BER of the users at BS.

### A. Statistical modeling of the effective channels of the users

The optimized component,  $\gamma_{ii}$ , is a summation of cascaded i.i.d. Rayleigh RVs, as in (3), which can be modeled as a Gamma RV using moment matching according to the casual form of the central limit theorem (CLT) [21]. Since both  $h_{ii,l}$  and  $g_{i,l}$  in (3) are independent complex normal RVs with unit variances, the mean value of  $\gamma_{ii}$  can be derived using the mean formula of Rayleigh RV [21] as

$$\mathbb{E}(\gamma_{ii}) = \sqrt{\frac{P_i \eta_i}{\beta_i}} L_i \mathbb{E}(|h_{ii,l}| |g_{i,l}|) = \sqrt{\frac{P_i \eta_i}{\beta_i}} \frac{\pi}{4} L_i. \quad (5)$$

Moreover, since the variance of the product of two Rayleigh RVs,  $|h_{ii,l}| |g_{i,l}|$ , when both  $|h_{ii,l}|$  and  $|g_{i,l}|$  are  $\mathcal{CN}(0, 1)$ , is  $\frac{16-\pi^2}{16}$  [22], the variance of  $\gamma_{ii}$  can be calculated as

$$\text{Var}(\gamma_{ii}) = \frac{P_i \eta_i}{\beta_i} \frac{16 - \pi^2}{16} L_i. \quad (6)$$

Let us define the scale and shape parameters of the equivalent Gamma RV by  $\zeta$  and  $N$ , respectively. Then,  $\gamma_{ii}$  has a mean value of  $N\zeta$  and a variance of  $N\zeta^2$  [21]. Therefore, by equating the mean and variance of  $\gamma_{ii}$  to the mean and variance of the Gamma RV, both the scale and shape parameters of the Gamma RV can be derived as

$$\zeta_i = \sqrt{\frac{P_i \eta_i}{\beta_i}} \frac{16 - \pi^2}{4\pi}, \quad N_i = L_i \frac{\pi^2}{16 - \pi^2}. \quad (7)$$

Finally, the characteristic function (CF) of  $\gamma_{ii}$  can be given as

$$\Phi_{\gamma_{ii}}(z) = (1 - j' \zeta_i z)^{-N_i}. \quad (8)$$

On the other hand, the random components of the effective uplink channels,  $\gamma_{ij}$ , have different statistical distributions, which we derive in the following. Without loss of generality, by setting  $P_i$ ,  $\eta_i$  and  $\beta_i$  to unity, the normalized random components of the uplink channels,  $\hat{\gamma}_{ij}$ , can be expressed as

$$\hat{\gamma}_{ij} = \sum_{l=1}^{L_j} h_{ij,l} e^{j\theta_{j,l}} g_{j,l}, \quad \forall i, j, i \neq j. \quad (9)$$

Clearly,  $\hat{\gamma}_{ij}$  is an  $L_j$ -sum of the product of independent complex RVs, which makes  $\hat{\gamma}_{ij}$  another complex RV having real and imaginary components. The following proposition

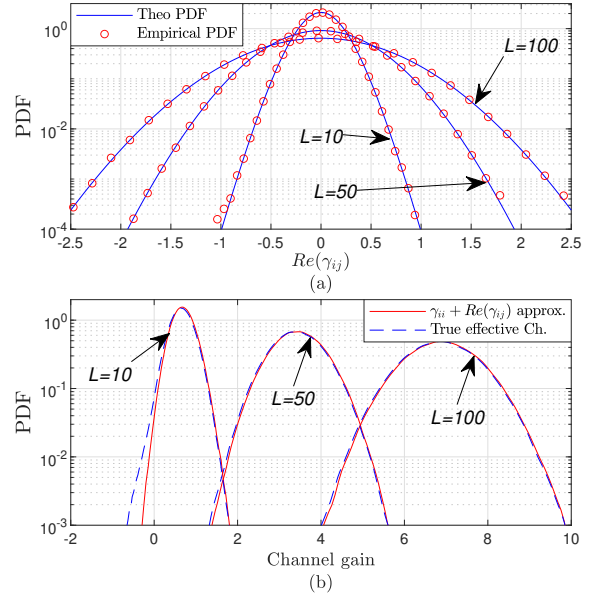


Figure 2: Comparison between the empirical and theoretical channels' PDFs of a two-user system under different values of  $L$ ,  $d_{U_1,I} = 20$ ,  $d_{U_2,I} = 50$ ,  $d_{I,B} = 30$ ,  $\psi = 2.2$ , and  $P_1 = P_2 = 40$  dB: (a) PDF of  $\Re(\gamma_{ij})$ , (b) PDF of the effective channel of  $U_i$  after channel alignment.

gives the statistical distribution of both the real and imaginary components of  $\hat{\gamma}_{ij}$ .

**Proposition 1.** *The real and imaginary parts of  $\hat{\gamma}_{ij}$  are identically distributed RVs where each of them can be modeled as a difference between two i.i.d. Erlang distributions with shape and scale parameters of  $L_j$  and 0.5, respectively. Therefore, the CF of  $\Re(\hat{\gamma}_{ij})$  can be given as*

$$\Phi_{\Re(\hat{\gamma}_{ij})}(z) = (1 + 0.25z^2)^{-L_j}.$$

*Proof.* See Appendix A. ■

Since  $\gamma_{ij}$  is just a scaled version of  $\hat{\gamma}_{ij}$  with a scale factor of  $\sqrt{\frac{P_i \eta_i}{\beta_i}}$ , then the CF of  $\Re(\gamma_{ij})$  can be directly found by replacing every  $z$  with  $\sqrt{\frac{P_i \eta_i}{\beta_i}} z$  in  $\Phi_{\Re(\hat{\gamma}_{ij})}(z)$  as

$$\Phi_{\Re(\gamma_{ij})}(z) = \Phi_{\Re(\hat{\gamma}_{ij})}\left(\sqrt{\frac{P_i \eta_i}{\beta_i}} z\right) = \left(1 + \frac{P_i \eta_i}{4\beta_i} z^2\right)^{-L_j}. \quad (10)$$

Figure Fig. 2(a) confirms that the derived theoretical probability density function (PDF) of  $\Re(\gamma_{ij})$  perfectly matches the empirical PDF using simulations with different values of  $L$ .

### B. Channel alignment scheme for the users' effective channels

In this subsection, we present an approach to align the overall effective channel of each user to the real axis by canceling the relatively small imaginary random components of the channel. This alignment scheme facilitates the efficient and simple detection of the uplink transmit data symbols of the users since it allows for simpler decision regions and decision thresholds. Moreover, obtaining closed-form expressions for

BER becomes feasible using the proposed channel alignment scheme, since the received signal constellation of the superimposed NOMA symbols at the BS becomes a QAM-like constellation, allowing tractable BER analysis.

To align the effective channels of the users in (2), let us define the angles,  $\alpha_j, \forall j \in \{1, \dots, K\}$ , as two control angles at the RIS. Specifically,  $\alpha_j$  is set to control the RIS partition,  $\mathcal{P}_j$ , by rotating all its elements by the same value of  $\alpha_j$ . Therefore, the received superimposed NOMA signal at the BS can be expressed as

$$y = \sum_{i=1}^K \sum_{j=1}^K \gamma_{ij} e^{j' \alpha_j} x_i + n. \quad (11)$$

The angles  $\alpha_j, \forall j$  are set so that they cancel the imaginary components of the overall effective channels of all the users,  $h_i^{eff}, \forall i \in \{1, \dots, K\}$ . Hence,  $\alpha_j, \forall j$  are calculated by simultaneously solving the following equations

$$\Im \left( \sum_{j=1}^K \gamma_{ij} e^{j' \alpha_j} \right) = 0, \quad \forall i \in \{1, 2, \dots, K\}, \quad (12)$$

where the system of equations in (12) consists of  $K$  nonlinear equations in  $K$  unknown angles,  $\alpha_j, \forall j$ , which can be numerically solved using a numerical technique such as Newton's method.

Since the optimized components,  $\gamma_{ii}, \forall i$ , have much higher magnitude than the random components,  $\gamma_{ij}, \forall i \neq j$ , the solution for (12) would normally have small values for  $\alpha_j, \forall j$ . In other words, the overall effective channels of the users can be aligned by adding a slight phase rotation to each RIS partition, which allows the large optimized channel components,  $\gamma_{ii}, \forall i$ , to dominate the small random components,  $\gamma_{ij}, \forall i \neq j$ . Thus, the overall effective channels of the users,  $h_i^{eff}, \forall i$ , become purely real after applying the control angles,  $\alpha_j$ , and they can be written as

$$h_i^{eff} = \sum_{j=1}^K \gamma_{ij} e^{j' \alpha_j} \approx \gamma_{ii} + \sum_{\substack{j=1 \\ j \neq i}}^K \text{Re}(\gamma_{ij}), \quad \forall i \in \{1, \dots, K\}, \quad (13)$$

where  $\approx$  means approximately equal. This approximation is validated using Monte-Carlo simulations in Fig. 2(b), where we compare the true empirical PDF of the effective channel to the approximate statistical model in (13). Therefore, the CF of  $h_i^{eff}, \forall i$ , can be given using (8) and (10) as

$$\Phi_{h_i^{eff}}(z) \approx \Phi_{\gamma_{ii}}(z) \prod_{j=1, j \neq i}^K \left( 1 + \frac{P_i \eta_j}{4\beta_i} z^2 \right)^{-L_j}. \quad (14)$$

The final received signal at the BS can then be expressed as

$$y = \sum_{i=1}^K h_i^{eff} x_i + n, \quad (15)$$

where  $h_i^{eff}, \forall i$  are purely real RVs with zero phase rotations. In the next subsection, we show how the proposed channel alignment scheme facilitates the detection process and the BER analysis.

### III. BER ANALYSIS OF THE TWO-USER UPLINK RIS-NOMA SYSTEM

In this section, we provide a comprehensive BER analysis for the two-user RIS-NOMA scenario, assuming 16-QAM and quadrature phase shift keying (QPSK) modulation for  $U_1$  and  $U_2$ , respectively. Gray coding is employed to map binary bits to QPSK symbols, with the mapping as follows:  $00 \rightarrow s_0$ ,  $01 \rightarrow s_1$ ,  $10 \rightarrow s_2$ , and  $11 \rightarrow s_3$ . Each QPSK symbol's first and second bits are denoted as  $b_{n1}$  and  $b_{n2}$  respectively, where  $n \in \{1, 2\}$  represents the  $n$ th user.

The symbols,  $x_1$  and  $x_2$ , are jointly decoded from (15) based on the construction of the received superimposed NOMA symbol constellation at the BS. Given that the receiver noise,  $n$ , is circularly symmetric Gaussian, optimal detection simplifies to a minimum distance decoder based on the effective channel values,  $h_i^{eff}, \forall i$ . With zero phase rotations of the effective channels, the decision regions for the superimposed NOMA symbols are simple rectangular shapes, akin to standard QAM detection. This QAM-like constellation structure facilitates simple and tractable data decoding through simple thresholds and decision regions. Therefore, the decision thresholds can be calculated given  $h_1^{eff}$  and  $h_2^{eff}$ , as we show below. It should be noted that constructing simple and tractable decision regions facilitates the derivation of closed-form BER analytical expressions, which will be used later in optimizing the uplink PA to mitigate the ambiguity of the superimposed constellation of uplink NOMA and its associated BER floors.

The constellation of the 16-4-QAM NOMA symbols of the two-user system is shown in Fig. 3. The combined constellation diagram of the NOMA symbol in this case has 64 constellation points containing an information amount of 6 bits per symbol, that is, four bits for  $U_1$  and two bits for  $U_2$ . Figure 3(a) divides the constellation points into two sets according to the value of  $b_{11}$  equal to 1 or 0, that is, the constellation points that have  $b_{11} = 0$  are red colored, while the remaining points having  $b_{11} = 1$  are in blue. Figure 3(b) divides the constellation diagram in the same way as Fig. 3(a) but according to  $b_{12}$ . For  $b_{13}$  and  $b_{14}$ , the constellation points are divided exactly in the same way as  $b_{11}$  and  $b_{12}$ , respectively, but horizontally not vertically. On the other hand, Fig. 3(c) shows the division of the constellation points according to the value of  $b_{21}$  being 1 or 0. For the second bit of  $U_2$ ,  $b_{22}$ , the constellation diagram is divided in the same way as in Fig. 3(c) but horizontally not vertically.

Since Fig. 3 clearly divides the constellation into decision regions according to each bit, we will use it to derive the average BER expressions for both  $U_1$  and  $U_2$  using a set of decision thresholds denoted by  $\lambda_i$  which can be given as

$$\lambda_0 = 0, \quad \lambda_i = \frac{\delta_i + \delta_{i+1}}{2}, \quad \forall i \in \{1, 2, 3\}, \quad (16)$$

where the values of the  $\delta$ 's are given as

$$\begin{aligned} \delta_1 &= h_1^{eff} - h_2^{eff}, & \delta_2 &= h_1^{eff} + h_2^{eff}, \\ \delta_3 &= 3h_1^{eff} - h_2^{eff}, & \delta_4 &= 3h_1^{eff} + h_2^{eff}. \end{aligned} \quad (17)$$

In the following BER calculations, we assume that  $\delta_4 > \lambda_3 > \delta_3 > \lambda_2 > \delta_2 > \lambda_1 > \delta_1 > 0$ . Although these values depend

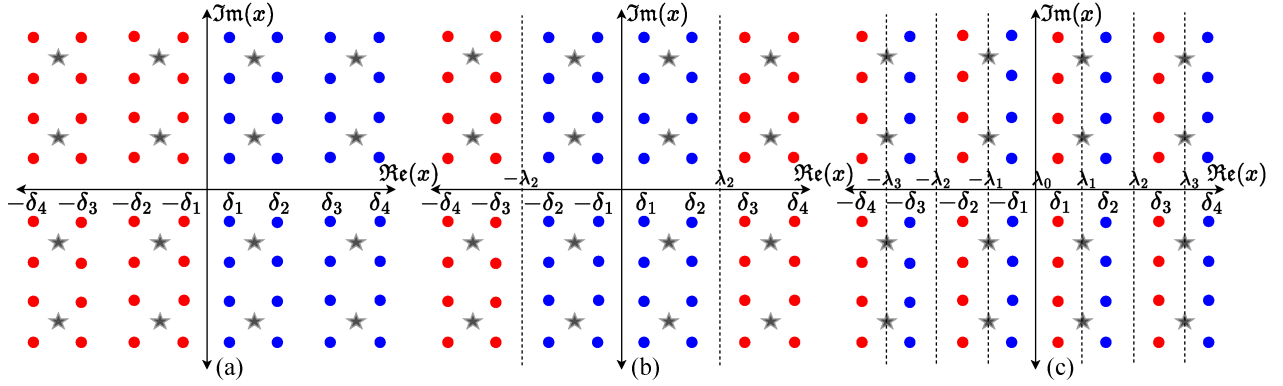


Figure 3: Combined uplink NOMA constellations for the 2-user 16-QAM system: (a)  $b_{11}$ , (b)  $b_{12}$ , (c)  $b_{21}$ .

on the values of the effective channels,  $h_i^{eff}$ , which are RVs by nature, we derive all the BER expressions assuming this desired order. The rationale of this choice is driven by the fact that this order can be achieved with optimized uplink PA based on minimizing the obtained BER expressions. This uplink PA will ensure that the correct order is satisfied by reducing the channel ambiguity among the users, as it heavily penalizes the average BER cost function.

#### A. Analysis of $U_1$

To calculate the average BER of  $U_1$ , we need to calculate the average probability of detection error of its individual bits,  $b_{1i}, \forall i \in \{1, \dots, 4\}$ , and take the average over these probabilities. Let us assume that the columns of the constellation diagrams in Fig. 3 are numbered from left to right as  $C_1, \dots, C_8$ . Starting with  $b_{11}$ , a detection error can occur if any of the blue constellation points in Fig. 3(a) moves to the negative side of the real axis or if any of the red points moves to the positive side. For example, assuming that the true received constellation point belongs to the fifth column,  $C_5$ , and given  $h_i^{eff}$ , the conditional error probability of  $b_{11}$  can be expressed as

$$P_{b_{11}|h_i^{eff}, C_5} = \Pr(\Re(n) < -\delta_1) = Q\left(\frac{\delta_1}{\sigma_n}\right), \quad (18)$$

where  $Q(x) \triangleq \frac{1}{\sqrt{2\pi}} \int_x^\infty e^{-u^2/2} du$ . Similarly, the conditional error probability of  $b_{11}$  can be calculated, given that the received constellation point belongs to any of the other columns,  $C_m, \forall m$ . Hence, the average bit error probability of  $b_{11}$ , averaged over all  $C_m, \forall m \in \{1, \dots, 8\}$ , can be calculated as

$$P_{b_{11}|h_i^{eff}} = \frac{1}{4} \sum_{m=1}^4 Q\left(\frac{\delta_m}{\sigma_n}\right). \quad (19)$$

On the other hand, we can notice from Fig. 3(b) that a detection error can occur in detecting the second bit of  $U_1$ ,  $b_{12}$ , if any of the blue points exceeds the decision region bounds, that is, from  $-\lambda_2$  to  $\lambda_2$  on the real axis, or if any of the red points enters that region. Hence, to calculate the detection error probability of  $b_{12}$ , we calculate the conditional error probability given that the received constellation point belongs to each of the columns, and then we take the average over all possible columns.

Given that the true received constellation point belongs to  $C_1$ , the conditional error probability of detecting  $b_{12}$  can be calculated as

$$\begin{aligned} P_{b_{12}|h_i^{eff}, C_1} &= \Pr(-\lambda_2 + \delta_4 < \Re(n) < \lambda_2 + \delta_4) \\ &= Q\left(\frac{-\lambda_2 + \delta_4}{\sigma_n}\right) - Q\left(\frac{\lambda_2 + \delta_4}{\sigma_n}\right). \end{aligned} \quad (20)$$

Similarly, if the received constellation point belongs to  $C_m$ , the conditional error probability of detecting  $b_{12}$  can be calculated as

$$\begin{aligned} P_{b_{12}|h_i^{eff}, C_m} &= \Pr\left(\Re(n) > (-1)^{\lceil \frac{m}{2} \rceil} \lambda_2 + \delta_{5-m}, \right. \\ &\quad \left. \Re(n) < (-1)^{\lceil \frac{m}{2} \rceil + 1} \lambda_2 + \delta_{5-m}\right) \\ &= (-1)^{\lceil \frac{m}{2} \rceil} Q\left(\frac{\lambda_2 + (-1)^{\lceil \frac{m}{2} \rceil + 1} \delta_{5-m}}{\sigma_n}\right) \\ &\quad + Q\left(\frac{(-1)^{\lceil \frac{m}{2} \rceil} \lambda_2 + \delta_{5-m}}{\sigma_n}\right), \quad \forall m \in \{1, 2, 3, 4\}. \end{aligned} \quad (21)$$

Due to symmetry in Fig. 3(b), it is clear that the cases of  $C_5, C_6, C_7$  and  $C_8$  are similar to the cases of  $C_4, C_3, C_2$  and  $C_1$ , respectively. Therefore, the average detection error probability of  $b_{12}$  can be obtained by averaging over the first four columns as

$$P_{b_{12}|h_i^{eff}} = \frac{1}{4} \sum_{m=1}^4 P_{b_{12}|h_i^{eff}, C_m}. \quad (22)$$

Finally, since  $b_{13}$  and  $b_{14}$  are similar to  $b_{11}$  and  $b_{12}$ , the conditional average BER of  $U_1$  given the values of the effective channels,  $h_i^{eff}$ , can be calculated by taking the average of the error probabilities of  $b_{11}$  and  $b_{12}$  as

$$P_{U_1|h_i^{eff}} = 0.5(P_{b_{11}|h_i^{eff}} + P_{b_{12}|h_i^{eff}}), \quad (23)$$

where  $P_{b_{11}|h_i^{eff}}$  and  $P_{b_{12}|h_i^{eff}}$  are given in (19) and (22), respectively.

#### B. Analysis of $U_2$

To calculate the average BER of  $U_2$ , we need to calculate the probability of detection error of its two individual bits,  $b_{21}$  and  $b_{22}$ , then taking the average of them. Figure 3(c) shows the constellation mapping of  $b_{21}$ , where the blue points represent



$b_{21} = 1$  while the red points represent having  $b_{21} = 0$ . The constellation mapping of  $b_{22}$  is exactly the same as shown in Fig. 3(c) but horizontally not vertically. Hence,  $b_{21}$  and  $b_{22}$  have similar detection error probabilities due to the symmetry of their constellation mappings, which makes the average BER of  $U_2$  equal to the probability of detection error of  $b_{21}$ .

From Fig. 3(c), an error can occur when detecting  $b_{21}$  if any of the blue constellation points moves to the decision regions of the red points or vice versa. To calculate the total average detection error probability of  $b_{21}$ , we derive the conditional error probability given that the received constellation point belongs to  $C_i$ , then we take the average over all the possible 8 columns. However, due to the symmetry between the red columns and the blue columns in Fig. 3(c), we only calculate the conditional error probability given  $C_1, C_3, C_5$  and  $C_7$ , and then we take the average over them.

Assuming that the true received constellation point belongs to  $C_1$ , and given  $h_i^{eff}$ , the conditional error probability of  $b_{21}$  can be expressed as

$$\begin{aligned} P_{b_{21}|h_i^{eff}, C_1} &= \Pr\left(\Re\{n\} \in \{[-\lambda_3 + \delta_4, -\lambda_2 + \delta_4] \cup \right. \\ &\quad \left. [-\lambda_1 + \delta_4, \delta_4] \cup [\lambda_1 + \delta_4, \lambda_2 + \delta_4] \cup [\lambda_3 + \delta_4, \infty]\right\}) \\ &= Q\left(\frac{-\lambda_3 + \delta_4}{\sigma_n}\right) - Q\left(\frac{-\lambda_2 + \delta_4}{\sigma_n}\right) + Q\left(\frac{-\lambda_1 + \delta_4}{\sigma_n}\right) \\ &\quad - Q\left(\frac{\delta_4}{\sigma_n}\right) + Q\left(\frac{\lambda_1 + \delta_4}{\sigma_n}\right) - Q\left(\frac{\lambda_2 + \delta_4}{\sigma_n}\right) + Q\left(\frac{\lambda_3 + \delta_4}{\sigma_n}\right). \end{aligned} \quad (24)$$

If the received constellation point belongs to  $C_3$ , the conditional error probability of detecting  $b_{21}$  can be expressed as

$$\begin{aligned} P_{b_{21}|h_i^{eff}, C_3} &= \Pr\left(\Re\{n\} \in \{[-\lambda_3 + \delta_2, -\lambda_2 + \delta_2] \cup \right. \\ &\quad \left. [-\lambda_1 + \delta_2, \delta_2] \cup [\lambda_1 + \delta_2, \lambda_2 + \delta_2] \cup [\lambda_3 + \delta_2, \infty]\right\}) \\ &= Q\left(\frac{-\lambda_3 + \delta_2}{\sigma_n}\right) - Q\left(\frac{-\lambda_2 + \delta_2}{\sigma_n}\right) + Q\left(\frac{-\lambda_1 + \delta_2}{\sigma_n}\right) \\ &\quad - Q\left(\frac{\delta_2}{\sigma_n}\right) + Q\left(\frac{\lambda_1 + \delta_2}{\sigma_n}\right) - Q\left(\frac{\lambda_2 + \delta_2}{\sigma_n}\right) + Q\left(\frac{\lambda_3 + \delta_2}{\sigma_n}\right). \end{aligned} \quad (25)$$

In the case of receiving a constellation point that belongs to  $C_5$ , the conditional error probability of detecting  $b_{21}$  can be given as

$$\begin{aligned} P_{b_{21}|h_i^{eff}, C_5} &= \Pr\left(\Re\{n\} \in \{[-\lambda_3 - \delta_1, -\lambda_2 - \delta_1] \cup \right. \\ &\quad \left. [-\lambda_1 - \delta_1, -\delta_1] \cup [\lambda_1 - \delta_1, \lambda_2 - \delta_1] \cup [\lambda_3 - \delta_1, \infty]\right\}) \\ &= Q\left(\frac{-\lambda_3 - \delta_1}{\sigma_n}\right) - Q\left(\frac{-\lambda_2 - \delta_1}{\sigma_n}\right) + Q\left(\frac{-\lambda_1 - \delta_1}{\sigma_n}\right) \\ &\quad - Q\left(\frac{-\delta_1}{\sigma_n}\right) + Q\left(\frac{\lambda_1 - \delta_1}{\sigma_n}\right) - Q\left(\frac{\lambda_2 - \delta_1}{\sigma_n}\right) + Q\left(\frac{\lambda_3 - \delta_1}{\sigma_n}\right). \end{aligned} \quad (26)$$

When the received constellation point belongs to  $C_7$ , the conditional error probability of detecting  $b_{21}$  can be calculated

as

$$\begin{aligned} P_{b_{21}|h_i^{eff}, C_7} &= \Pr\left(\Re\{n\} \in \{[-\lambda_3 - \delta_3, -\lambda_2 - \delta_3] \cup \right. \\ &\quad \left. [-\lambda_1 - \delta_3, -\delta_3] \cup [\lambda_1 - \delta_3, \lambda_2 - \delta_3] \cup [\lambda_3 - \delta_3, \infty]\right\}) \\ &= Q\left(\frac{-\lambda_3 - \delta_3}{\sigma_n}\right) - Q\left(\frac{-\lambda_2 - \delta_3}{\sigma_n}\right) + Q\left(\frac{-\lambda_1 - \delta_3}{\sigma_n}\right) \\ &\quad - Q\left(\frac{-\delta_3}{\sigma_n}\right) + Q\left(\frac{\lambda_1 - \delta_3}{\sigma_n}\right) - Q\left(\frac{\lambda_2 - \delta_3}{\sigma_n}\right) + Q\left(\frac{\lambda_3 - \delta_3}{\sigma_n}\right). \end{aligned} \quad (27)$$

Thus, the average BER of  $U_2$  given the effective channels,  $h_i^{eff}$ , can be calculated as

$$P_{U_2|h_i^{eff}} = P_{b_{21}|h_i^{eff}} = \frac{1}{4} \sum_{m=0}^3 P_{b_{21}|h_i^{eff}, C_{2m+1}}, \quad (28)$$

where  $P_{b_{21}|h_i^{eff}, C_{2m+1}}$  for  $m = 0, 1, 2$ , and  $3$  is given in (24), (25), (26), and (27), respectively.

After deriving the conditional BERs given the instantaneous effective channels of the users, the derivation of the average unconditional BER expressions of  $U_1$  and  $U_2$  is presented in Sec. IV-B. This is performed by averaging the expressions obtained in (23) and (28), respectively, over the PDFs of the effective channels,  $h_1^{eff}$  and  $h_2^{eff}$ .

#### IV. DESIGN AND BER ANALYSIS OF THE GENERALIZED $K$ -USER $M$ -QAM UPLINK RIS-NOMA SYSTEM

In this section, a framework is presented for deriving closed-form BER expressions for the generalized uplink RIS-NOMA system with an arbitrary number of users and arbitrary QAM modulation orders. Specifically, we extend our BER analysis to the generalized system by specifically providing an algorithm that calculates the coefficients of the BER expressions for an arbitrary number of users and QAM modulation orders. Then, we provide a methodology to derive the unconditional average BER expressions of the generalized system by averaging over the CFs of the effective channels of the  $K$  users.

##### A. Generalization for arbitrary number of users and QAM modulation orders

In this subsection, we generalize our analysis by devising a methodology to obtain the BER expressions for a general uplink RIS-NOMA system with arbitrary number of users and arbitrary QAM modulation orders for the users. From Sec. III, we have found that the conditional BER expressions always take the form of a weighted sum of  $Q(\cdot)$  functions having different linear combinations of the effective channels,  $h_i^{eff}$ , as arguments. Consequently, for a general  $K$ -user system, the conditional BER expression of user  $k$ , given the effective channel values,  $h_i^{eff}, \forall i$ , can be expressed as

$$BER_{U_k|h_1^{eff}, \dots, h_K^{eff}} = \sum_{q=1}^{N_k} c_{k,q} Q\left(\frac{\sum_{i=1}^K a_{k,iq} h_i^{eff}}{\sigma_n}\right), \quad (29)$$

where  $N_k$  is the total number of  $Q(\cdot)$  functions in the BER expression of  $U_k$ , while the coefficients  $c_{k,q}$  and  $a_{k,iq}$  depend on the number of users,  $K$ , and the QAM modulation orders

used by these users. Therefore, by devising an algorithm that can compute these coefficients for arbitrary number of users and QAM modulation orders, we can calculate the conditional BER expressions for a generalized uplink RIS-NOMA system.

Due to applying the proposed channel alignment scheme in Sec. II-B, the received superimposed uplink NOMA constellation at the BS is constructed as the constellation of downlink NOMA systems. Therefore, utilizing the proposed channel alignment scheme allows us to use the methodology provided in Sec. III of [23] for deriving the generalized BER expressions of downlink NOMA systems. Section III of [23] provides a methodology to obtain the weights of the  $Q(\cdot)$  functions,  $c_{k,q}$ , in (29), but does not calculate the coefficients,  $a_{k,iq}$ , which are inside the  $Q(\cdot)$  functions. The reason for this is that, unlike uplink NOMA systems, the constellation of downlink NOMA systems experiences only one fading channel before reception at the user, where the signal received at the  $k$ th user can be given as

$$y_k = \left( \sum_{i=1}^K \sqrt{\rho_i} x_i \right) h_k + n_k, \quad (30)$$

where  $\rho_i$  is the power allocated to user  $i$ , while  $h_k$  and  $n_k$  are the fading channel and additive white Gaussian noise (AWGN) of the  $k$ th user, respectively. However, the methodology in [23] calculates the error distances of the downlink NOMA constellation which can be written as

$$\Delta_{k,q} = \sum_{i=1}^K a_{k,iq} \sqrt{\rho_i}, \quad (31)$$

where  $a_{k,iq}, \forall i, q$  are the required coefficients for the  $k$ th user in (29). Hence, setting  $\rho_i$  to some known values, we can compute the coefficients,  $a_{k,iq}$ , of the  $k$ th user by knowing the distances,  $\Delta_{k,q}$ , using **Algorithm 1**. The  $i$ th element of the input vector,  $\mathbf{b}$ , of **Algorithm 1** is the number of bits per symbol of the  $i$ th user,  $b_i$ , representing its modulation order, while  $\boldsymbol{\rho}$  contains the power coefficients of the users,  $\rho_i, \forall i$ . The vector,  $\boldsymbol{\Delta}_k$ , contains all the error distances of the  $k$ th user,  $\Delta_{k,q}, \forall q$ . The output of **Algorithm 1** are the matrices,  $\mathbf{A}_1, \dots, \mathbf{A}_K$ , which contain the required coefficients,  $a_{k,iq}, \forall i, q$ , that is, the element of the  $q$ th row and the  $i$ th column of  $\mathbf{A}_k$  is  $a_{k,iq}$ .

The idea of **Algorithm 1** is that the coefficient,  $a_{iq}$ , in (31) can be calculated using the partial differentiation of  $\Delta_{k,q}$  with respect to (w.r.t.)  $\sqrt{\rho_i}$ . Since  $\Delta_{k,q}$  is a linear function in  $\sqrt{\rho_i}$ , then the partial derivative of  $\Delta_{k,q}$  w.r.t.  $\sqrt{\rho_i}$  can be calculated as

$$a_{k,iq} = \mathbf{A}_k(q, i) = \frac{\partial \Delta_{k,q}}{\partial \sqrt{\rho_i}} = \frac{\Delta_{k,q}^{(2)} - \Delta_{k,q}^{(1)}}{\sqrt{\rho_i}^{(2)} - \sqrt{\rho_i}^{(1)}}, \quad \forall k, i, q. \quad (32)$$

The power coefficients,  $\rho_i$ , are set in **Algorithm 1** as  $\rho_i = 2^{\sum_{i+1}^K b_i}, \forall i < K$  and  $\rho_K = 1$ , because this setting prevents overlapping between the superimposed NOMA constellation points.

---

**Algorithm 1:** Calculation of  $a_{k,iq}, \forall k, i, q$ .

---

```

1 Inputs:  $\mathbf{b}$  and  $\boldsymbol{\rho}$ .
2 for  $k=1:K$  do
3   Calculate  $\boldsymbol{\Delta}_k^{(1)}$  using the method in [23], with
   inputs  $\mathbf{b}$  and  $\boldsymbol{\rho}$ .
4   for  $i = 1 : K$  do
5     Set  $\varepsilon$  to any small value, e.g.,  $\varepsilon = 0.1$ ;
6     Set  $\boldsymbol{\rho}' = \boldsymbol{\rho}$ ;
7     Set  $\boldsymbol{\rho}'(i) = \left( \sqrt{\rho(i)} + \varepsilon \right)^2$ ;
8     Calculate  $\boldsymbol{\Delta}_k^{(2)}$  using the method in [23], with
     inputs  $\mathbf{b}$  and  $\boldsymbol{\rho}'$ .
9     for  $q = 1 : \text{length}(\boldsymbol{\Delta}_k^{(1)})$  do
10       $\mathbf{A}_k(q, i) = \frac{\Delta_k^{(2)}(q) - \Delta_k^{(1)}(q)}{\varepsilon}$ ;
11    end
12  end
13 end
14 Return:  $\mathbf{A}_1, \mathbf{A}_2, \dots, \mathbf{A}_K$ .

```

---

*B. Averaging the BER expressions over the PDFs of the RIS effective channels*

In this subsection, we provide a methodology to average the obtained conditional BER expressions in (29) over the PDFs of  $h_i^{eff}, \forall i$ . However, the random channel components,  $\Re(\gamma_{ij}), i \neq j$ , are correlated since they contain common RIS-BS channel coefficients,  $\mathbf{g}_j$ . For example, in the three-user scenario, the argument inside the  $q$ th  $Q(\cdot)$  function of the BER expression of the  $k$ th user can always be expressed as

$$\begin{aligned} X_{k,q} &= a_{k,1q} h_1^{eff} + a_{k,2q} h_2^{eff} + a_{k,3q} h_3^{eff} \\ &\approx \tilde{a}_{k,1q} \left( \sum_{l=1}^{L_1} |h_{11,l}| |g_{1,l}| + \Re(\tilde{\mathbf{g}}_2^T \mathbf{h}_{12} + \tilde{\mathbf{g}}_3^T \mathbf{h}_{13}) \right) \\ &+ \tilde{a}_{k,2q} \left( \sum_{l=1}^{L_2} |h_{22,l}| |g_{2,l}| + \Re(\tilde{\mathbf{g}}_1^T \mathbf{h}_{21} + \tilde{\mathbf{g}}_3^T \mathbf{h}_{23}) \right) \\ &+ \tilde{a}_{k,3q} \left( \sum_{l=1}^{L_3} |h_{33,l}| |g_{3,l}| + \Re(\tilde{\mathbf{g}}_1^T \mathbf{h}_{31} + \tilde{\mathbf{g}}_2^T \mathbf{h}_{32}) \right), \end{aligned} \quad (33)$$

where  $\tilde{a}_{k,iq} = a_{k,iq} \sqrt{\frac{P_i \eta_i}{\beta_i}}$ , and  $\tilde{\mathbf{g}}_i = \boldsymbol{\Theta}_i \mathbf{g}_i$  where  $\boldsymbol{\Theta}_i$  is the diagonal reflection coefficients matrix of the  $i$ th partition,  $P_i$ . Now, we need to derive the CF of the compound RV,  $X$ , to use it to derive the average of  $Q(X)$ . However, the real components of (33) are correlated, since  $\tilde{g}_{1,l}, \tilde{g}_{2,l}$  and  $\tilde{g}_{3,l}$  are common factors in them. Consequently, the terms of  $X$  in (33) are rearranged in a way that puts them in the form of a sum of uncorrelated terms, as

$$\begin{aligned} X_{k,q} &\approx \sum_{i=1}^3 \tilde{a}_{k,iq} \sum_{l=1}^{L_i} |h_{ii,l}| |g_{i,l}| \\ &+ \Re(\tilde{\mathbf{g}}_1^T (\tilde{a}_{k,2q} \mathbf{h}_{21} + \tilde{a}_{k,3q} \mathbf{h}_{31}) + \tilde{\mathbf{g}}_2^T (\tilde{a}_{k,1q} \mathbf{h}_{12} + \tilde{a}_{k,3q} \mathbf{h}_{32}) \\ &+ \tilde{\mathbf{g}}_3^T (\tilde{a}_{k,1q} \mathbf{h}_{13} + \tilde{a}_{k,2q} \mathbf{h}_{23})). \end{aligned} \quad (34)$$

Now, the CF of  $X_{k,q}$  can be easily derived by multiplying the CF of the terms in (34). Since the absolute value terms



are summations of product of two Rayleigh RVs, they can be modeled as Gamma RVs having CFs as in (8). For the real value terms, each of them is equivalent in distribution to

$$S_i \triangleq \sqrt{\sum_{j=1, j \neq i}^3 |\tilde{a}_{k,jq}|^2} \Re(\tilde{\mathbf{g}}_i^T \hat{\mathbf{h}}_i), \quad (35)$$

where both  $\tilde{\mathbf{g}}_i$  and  $\hat{\mathbf{h}}_i$  are i.i.d.  $\mathcal{CN}(\mathbf{0}, \mathbf{I})$ . Since  $S_i$  is a real sum of products of two independent  $\mathcal{CN}(0, 1)$ , it can be modeled as a difference between two i.i.d. Erlang distributions as in Proposition 1. Finally, by induction for a general  $K$ -user system, the CF of  $X_{k,q}$  can be written using (8) and (10) as

$$\Phi_{X_{k,q}}(z) = \left( \prod_{i=1}^K (1 - j' a_{k,iq} \zeta_i z)^{-N_i} \right) \left( \prod_{i=1}^K \left( 1 + \frac{\kappa_i}{4} z^2 \right)^{-L_i} \right), \quad (36)$$

where  $\zeta_i$  and  $N_i$  are given in (7), and  $\kappa_i = \sum_{j=1, j \neq i}^K |\tilde{a}_{k,jq}|^2$ . Finally, Proposition 2 gives the final unconditional BER of  $U_k$ .

**Proposition 2.** *By averaging (29) over the statistical distributions of  $h_i^{eff}$ ,  $\forall i$ , the unconditional average BER of  $U_k$  can be given as*

$$BER_{U_k} = \sum_{q=1}^{N_k} \frac{c_{k,q}}{2} + \frac{c_{k,q}}{\pi} \int_0^\infty \Re \left( \frac{j' e^{-\frac{z^2}{2}}}{z} \Phi_{X_{k,q}} \left( \frac{z}{\sigma_n} \right) \right) dz.$$

*Proof.* Please see Appendix B. ■

## V. AVERAGE BER MINIMIZATION BASED POWER ALLOCATION SCHEME

In this section, we introduce an optimized uplink PA scheme for the RIS-NOMA system. The aim of this PA is to eliminate the BER floors that occur in SIC-based uplink NOMA systems. Specifically, the transmit powers of the users are optimized to minimize the overall average BER performance at the BS for all users while adhering to individual uplink transmit power constraints. The optimization process is clearer and more robust when conducted in the log-log domain, where both the power values to be optimized,  $P_k$ , and the cost function are expressed in dB. This transformation results in smoother numerical optimization and faster convergence when applying gradient descent-based optimization techniques to solve our problem. Therefore, the uplink PA problem can be formulated as

$$\min_{P_1, P_2, \dots, P_K} 10 \log_{10} \left( \sum_{k=1}^K BER_{U_k} \left( 10^{\frac{P_1}{10}}, \dots, 10^{\frac{P_K}{10}} \right) \right) \quad (37a)$$

$$\text{s.t. } P_k \leq P_{dBm}^{\max}, \quad \forall k, \quad (37b)$$

where  $P_{dBm}^{\max}$  represents the maximum available uplink transmit power in dBm, and  $BER_{U_k}$  in (37a) is the general BER formula of  $U_k$  given in Proposition 2.

We use a gradient-based method to solve (37) where the cost function along with the constraints are all continuous and have continuous first derivatives. To deal with the constraints,

we shall transform (37) into an unconstrained optimization problem by constructing the Lagrangian that is given as

$$L(\mathbf{p}, \xi_1, \dots, \xi_K) = f(\mathbf{p}) + \sum_{k=1}^K \xi_k (P_k - P_{dBm}^{\max}), \quad (38)$$

where  $\xi_k$  is the Lagrange multiplier that corresponds to the  $k$ th constraint,  $f$  is the cost function in (37), and  $\mathbf{p} = [P_1, \dots, P_K]^T$ . The Lagrangian in (38) is optimized using Newton's gradient-based method, utilizing the Hessian operator of the Lagrangian. Given that the constraints are linear functions, the Hessian in this case only includes the Hessian of the original objective function  $f$ , as it represents the second derivative of  $L$ . Therefore, the Hessian of  $L$  can be given as

$$\nabla^2 L = \nabla^2 f(\mathbf{p}), \quad (39)$$

where  $\nabla^2$  is the Laplacian operator or the second order differential operator. Newton's method is an iterative algorithm that is applied using a starting point  $\mathbf{p}_0$  in an iterative manner until convergence to the optimum point. The update rule in each iteration can be given as

$$\mathbf{p}_{n+1} = \mathbf{p}_n - [\nabla^2 f(\mathbf{p}_n)]^{-1} \nabla f(\mathbf{p}_n). \quad (40)$$

The Lagrange multipliers,  $\xi_k$ , in (38) are hyperparameters that are adjusted iteratively until convergence is reached. This involves repeatedly optimizing the Lagrangian, starting with initial values for  $\xi_k$ , which are updated in each iteration. Generally, we start with high values for  $\xi_k$  and modify them based on how much the constraints are satisfied in every iteration. If  $(P_k - P_{dBm}^{\max}) < 0$ , the corresponding Lagrange multiplier,  $\xi_k$ , should be decreased. Conversely, if  $(P_k - P_{dBm}^{\max}) > 0$ , indicating a constraint violation,  $\xi_k$  should be increased.

It is important to highlight that while the optimization process described above is iterative, it relies on the average channel statistics of the users rather than their instantaneous channel coefficients. This aspect simplifies the hardware implementation of the PA algorithm. Specifically, the PA problem outlined in (37) is defined solely by the users' channel variances,  $\sigma_k^2$ , and the average received noise power,  $\sigma_n^2$ , all of which exhibit long coherence times. This method ensures that the proposed PA strategy remains computationally efficient while providing minimized average BER performance for all NOMA users, making it suitable for real-world applications.

## VI. SIMULATION RESULTS

In this section, we provide simulation results for the achievable BER of the introduced system under different operating conditions. We also validate our derived expressions using Monte-Carlo simulations with  $10^7$  simulation runs. The BER performance of the users is plotted against the transmit power while the Gaussian noise variance in the real or imaginary dimensions is set to unity, i.e.,  $\sigma_n^2 = 1$ . It should be noted that the simulated BER is plotted up to  $BER = 10^{-7}$  due to the limitation on the number of Monte-Carlo runs, whereas the analytical solution provides insights into the BER for smaller than  $10^{-7}$  values.

Moreover, the achievable BER performance of the RIS-NOMA system is compared to the RIS-OMA counterpart

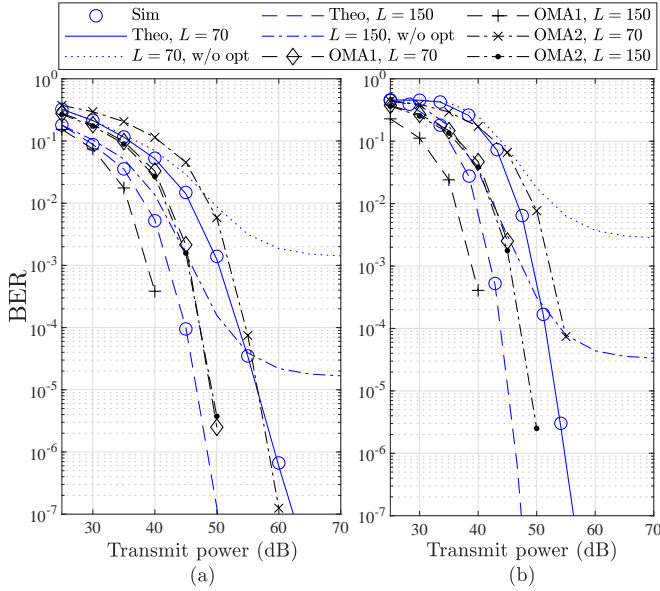


Figure 4: BER performance comparison between a 2-user RIS-NOMA system and the RIS-OMA counterpart under different  $L$  values and  $d_{U_1,I} = 20$ ,  $d_{U_2,I} = 70$ ,  $d_{I,B} = 30$ : (a)  $U_1$  (16-QAM), (b)  $U_2$  (4-QAM).

that applies time division multiple access (TDMA). For fair comparison, the time slot allocated to a certain user in RIS-TDMA-OMA scenario,  $T_{\text{OMA}}$ , equals the time slot in RIS-NOMA,  $T_{\text{NOMA}}$ , divided by the total number of users,  $K$ , i.e.,  $T_{\text{NOMA}} = KT_{\text{OMA}}$ . In addition, we fix the achievable data rate for all users by making the total number of bits transmitted by each user during  $T_{\text{OMA}}$  equal to the total number of bits transmitted by that user during  $T_{\text{NOMA}}$ . By way of explanation, the modulation order for user  $k$  in RIS-TDMA-OMA equals its modulation order in RIS-NOMA scenario raised to power  $K$ , which guarantees that the total number of transmitted bits in both systems is equal for the same amount of consumed network resources. In addition, two scenarios of OMA, named OMA1 and OMA2, have been adopted to achieve a fair comparison. In OMA1, all partitions, that is, all reflectors in the RIS panel, are assigned to each user during its signaling period, whereas only one partition is assigned to a certain user during its signaling time in OMA2, which is similar to the assignment when NOMA signaling is applied. It should be mentioned that in NOMA signaling, the total number of channels to be estimated is  $L = \sum_{i=1}^K L_i$ , which is equal to the number of phase shifts to be compensated at the RIS, while in OMA1, the total number of channels to be estimated and the number of compensated phase shifts is  $L \times K$ . Hence, OMA1 adds considerable limitations because of the extreme computational complexity imposed due to the high number of channels to be estimated and compensated at the RIS, as well as the phase switching speed at the RIS to update the phase shifts. Therefore, OMA2 is also considered in our simulations as another benchmark, which is more fair and practical since it requires the same number of channel estimates and phase compensations as the NOMA scenario.

Figure 4 shows the BER performance of a two-user uplink RIS-NOMA system model against the transmission power of

each user. The two users,  $U_1$  and  $U_2$ , employ QAM with orders of 16 and 4 in NOMA signaling, while they use modulation orders of 256 and 16, respectively, when TDMA-OMA is applied. Moreover, the users' distances to the RIS are 20 m and 70 m, respectively, while the RIS-BS distance is 30 m. The figure also compares the RIS-NOMA with RIS-OMA-TDMA under two values for the number of RIS reflectors per user. In the first case, a number of  $L_i = 70$  reflectors is assigned to each user, whereas  $L_i = 150$  reflectors are assigned to each user in the second case. As can be seen in the figure, without optimization (w/o opt), the RIS-NOMA system suffers from a significant error floor which increases as  $L$  decreases. For example, error floors in the BER of  $U_1$  of approximately  $1.5 \times 10^{-3}$  and  $1.5 \times 10^{-5}$  are observed when  $L_i$  is 70 and 150, respectively, while the error floors are about  $3 \times 10^{-3}$  and  $3 \times 10^{-5}$  for the second user. This error floor is attributed to the inter-user interference that dominates the AWGN at high SNR values. This error floor decreases when the number of RIS elements per user increases due to the signal-to-interference-plus-noise-ratio (SINR) enhancement gained by increasing  $L_i$ . However, as can be observed from the figure, the proposed PA algorithm in Sec. V has managed to eliminate the error floor by controlling the transmit power of each user, which in turn controls the amount of interference imposed by each user on other users. By comparing the performance of the optimized NOMA with TDMA-OMA1, it can be observed that the latter significantly outperforms NOMA even though higher modulation orders are applied in TDMA-OMA. For instance, Fig. 4(a) shows that there is a power gain of almost 7 dB in favor of TDMA-OMA1 at  $\text{BER} = 10^{-5}$  and  $L_i = 70$ , however, this gain decreases to about 2 dB as  $L_i$  increases to 150. This superiority of TDMA-OMA comes at the expense of considerably higher complexity due to channel estimation overheads, since all partitions are assigned to every user in TDMA-OMA1. On the other hand, by comparing NOMA with TDMA-OMA2 which has similar channel estimation overheads, it can be observed in Fig. 4 that, for  $U_2$ , NOMA outperforms TDMA-OMA2 for the whole range of SNR as shown in Fig. 4(b), and for a wide range of SNR values in Fig. 4(a) showing the BER of  $U_1$ . Finally, the figure shows a perfect match between the simulation results and the derived closed-form expressions, which confirms the accuracy of the analysis carried out in this paper.

Figure 5 shows the achievable BER for the same simulation parameters as Fig. 4 except from the distance of  $U_2$  which has been increased to 200 m in this figure. As can be seen in Fig. 5(a), increasing the distance of the second user,  $U_2$ , from the RIS reduces the interference on the first user,  $U_1$ , which also leads to a lower BER for  $U_1$ . Therefore, as shown in Fig. 5(b), when NOMA is applied,  $U_1$  performs better than TDMA-OMA1 and TDMA-OMA2 for the whole SNR range. However, the performance of  $U_2$  with TDMA-OMA1 is still better than that of NOMA. Comparing Fig. 4(b) to Fig. 5(b), it can be observed that  $U_2$  requires more power in the latter case to achieve the same BER in Fig. 4(b) due to the path loss imposed by long-distance transmission. Moreover, the results in Figs. 4 and 5 show that TDMA-OMA1 is generally preferred when low modulation orders are applied. However,

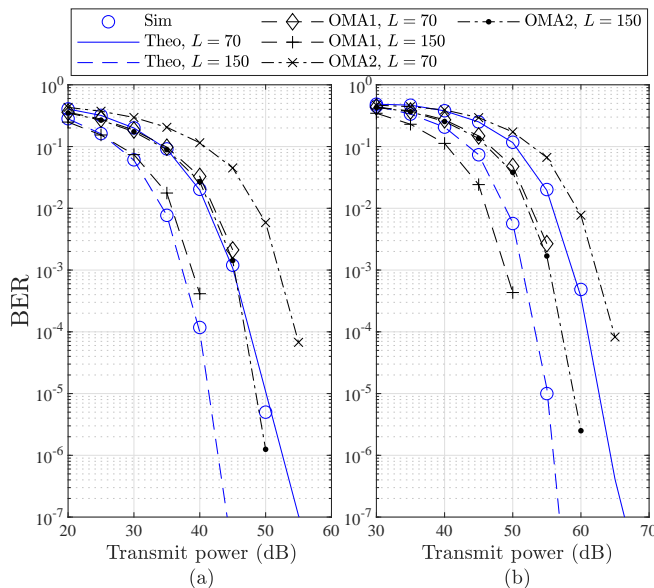


Figure 5: BER performance comparison between a 2-user RIS-NOMA system and the RIS-OMA counterpart under different  $L$  values and  $d_{U_1,I} = 20$ ,  $d_{U_2,I} = 200$ : (a)  $U_1$  (16 QAM), (b)  $U_2$  (4 QAM).

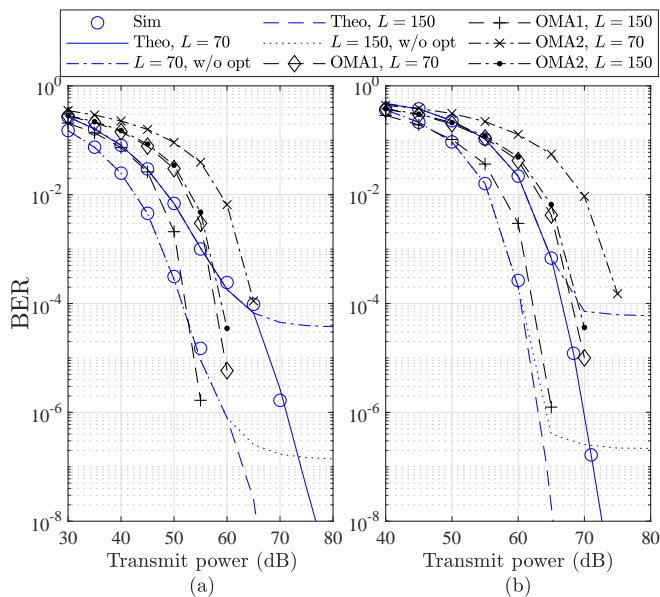


Figure 6: BER performance comparison between a 2-user RIS-NOMA system and the RIS-OMA counterpart under different  $L$  values and  $d_{U_1,I} = 20$ ,  $d_{U_2,I} = 200$ : (a)  $U_1$  (64 QAM), (b)  $U_2$  (16 QAM).

it should be noted that in TDMA-OMA1, each user can make use of all elements of the RIS, which imposes additional channel estimation overheads, unlike NOMA where the total number of reflectors is divided among users. Compared to TDMA-OMA2, which has the same channel estimation and phase compensation overheads as NOMA, the figure shows that NOMA is always preferable, as it provides lower BERs. The figure also shows a perfect match between the theoretical results and the simulation, which confirms the derivations carried out in this paper.

Figure 6 shows the achievable BER for the same simulation

parameters as Fig. 5, except for the modulation orders which have been increased to 64 and 16 for  $U_1$  and  $U_2$ , respectively, for the NOMA scenario, and  $2^{12}$  and  $2^8$  for  $U_1$  and  $U_2$ , respectively, in the TDMA-OMA scenario. As can be observed in the figure, similar to Fig. 4, optimized resources manage to remove the BER floor. In addition, it can be seen from the figure that as the modulation orders increase, the performance of the optimized NOMA becomes better than TDMA-OMA1 for the entire range of the transmit power of  $U_2$ , and for the low and mid ranges of the transmit power of  $U_1$ . For example, as can be seen from Fig. 6(a), the BER of  $U_1$  using TDMA-OMA intersects with the BER of NOMA at transmit powers of 53 dB and 56 dB for  $L_i = 150$  and  $L_i = 80$ , respectively, where TDMA-OMA1 performs better for a higher transmit power regime. On the other hand, it can be clearly seen from the figure that optimized NOMA manages to provide lower BER than TDMA-NOMA2 for both users and for the whole range of SNR. The figure also confirms the analytical expressions derived in this paper for the BER.

To verify the analysis of the generalized case with multiple users, in Fig. 7, we present the achievable BER performance of a three-user uplink RIS-NOMA scenario. The simulation parameters for  $U_1$  and  $U_2$  remain the same as in Fig. 6, except for the number of reflectors considered in the simulation setup where  $L = \{100, 200, 300\}$  have been assumed for NOMA. It should be noted that since each user uses the full potential of RIS in its time slot in the case of TDMA-OMA1, the equivalent number of reflectors in this case is  $L = \{300, 600, 900\}$ . The newly added  $U_3$  employs 16-QAM and is located at 2000 m from the RIS location. As can be observed from the figure, there is a perfect match between theoretical results and simulation for the three-user scenario, which confirms the derivations carried out in this paper. The figure also shows that increasing the number of reflectors significantly reduces the error floor of all users, while the error floor can be mitigated by using the PA algorithm introduced in this paper. Moreover, increasing the number of reflectors pushes the intersection points between the BER of NOMA and TDMA-OMA1 to be at much higher values of the transmit power. This in turn gives superiority to the optimized NOMA system over TDMA-OMA1 for a wide range of operating transmit power. For example, the BER of  $U_3$  achieved using the optimized NOMA is superior for the whole range of transmit power regardless  $L$ , and the superiority of the optimized NOMA over the considered range of the transmit power for  $U_1$  and  $U_2$  is achieved when  $L = \{200, 300\}$ . Moreover, when  $L = 100$ , this superiority is achieved for transmit power less than 68 dB for  $U_1$  and for transmit power less than 73 dB for  $U_2$ . Furthermore, comparing RIS-NOMA with the TDMA-OMA2 counterpart, it can be clearly observed that RIS-NOMA has superior performance for all users and for the entire operating SNR range.

## VII. CONCLUSIONS

This paper investigated the achievable performance of uplink RIS-NOMA system, where users transmit their data to the BS using the same resource block and the BS employs

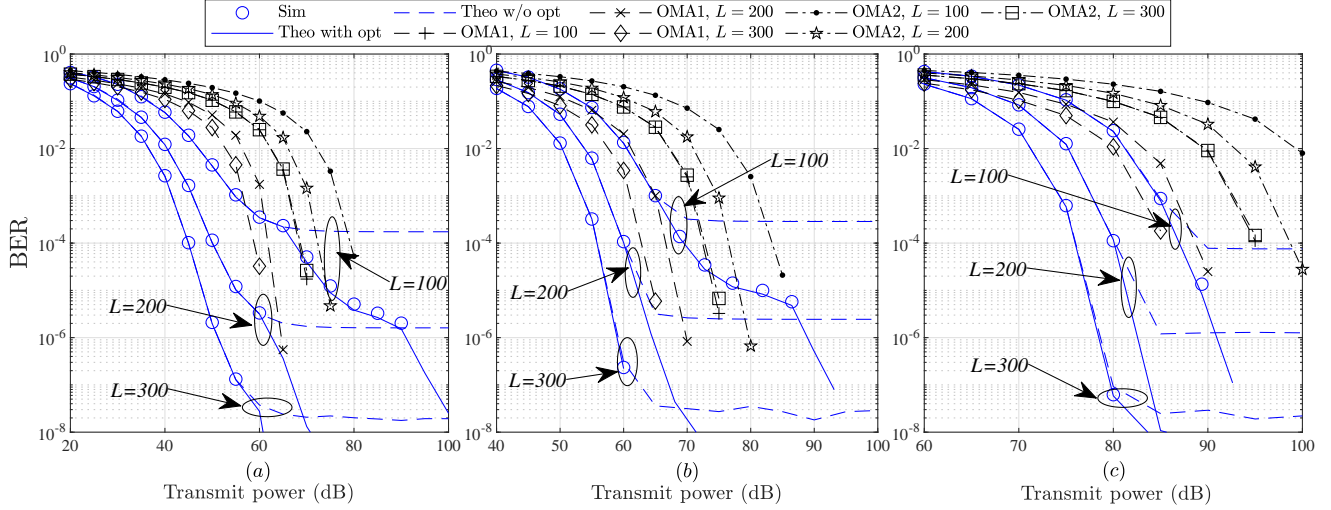


Figure 7: BER performance comparison between a 3-user RIS-NOMA system and the RIS-OMA counterpart under different  $L$  values and  $d_{U_{1,I}} = 20$ ,  $d_{U_{2,I}} = 200$ ,  $d_{U_{3,I}} = 2000$ : (a)  $U_1$  (64 QAM), (b)  $U_2$  (16 QAM), (c)  $U_3$  (16 QAM).

SIC to detect the data symbols of each user. Closed-form expressions for the achievable BER were derived to provide useful insights about the performance limits of RIS-NOMA. The BER was compared to two TDMA-OMA counterparts to provide a comprehensive and fair comparison, where the first utilizes all partitions for each user at the expense of extra complexity, whereas the other assigns a partition to each user. Furthermore, a PA algorithm was introduced to mitigate the error floor imposed by the inter-user interference of uplink NOMA.

Theoretical results corroborated by simulations revealed that RIS-NOMA is preferred over TDMA-OMA2 for almost all the considered SNR regimes. On the other hand, the benefits gained by NOMA could be limited compared to TDMA-OMA1 for low modulation orders and low numbers of reflectors, making TDMA-OMA1 able to outperform NOMA. The main reason for this is attributed to the fact that in TDMA-OMA1, each user can use the full potential of the RIS panel, i.e., each user is assigned all reflectors, while the reflectors are divided among users in NOMA. However, comparing NOMA to TDMA-OMA1 is not fair since the latter imposes a much larger channel estimation overhead on the system than the former. Thus, the gain of TDMA-OMA1 comes at the expense of considerable computational and hardware complexity imposed by channel estimation and RIS phase compensation for large numbers of reflectors. Moreover, in practice, there is a practical constraint on the phase-switching speed of the reflectors, which makes it impossible to allocate the same reflector to a different user in subsequent signaling times. Furthermore, it was shown that by increasing the number of reflectors and/or increasing the modulation order, NOMA can have superior performance compared to both TDMA-OMA scenarios for a wide range, and in some cases the whole range, of the transmit power.

#### APPENDIX A PROOF OF PROPOSITION 1

In this appendix, the CF of  $\Re(\hat{\gamma}_{ij})$ , where  $\hat{\gamma}_{ij}$  is given in (9), is derived. Assuming that  $\tilde{g}_{j,l} = e^{j\theta_{j,l}}g_{j,l}$ , we can say that  $\tilde{g}_{j,l}$  is still  $\mathcal{CN}(0, 1)$ . The reason for this fact is that  $\arg(\tilde{g}_{j,l}) \sim U(0, 2\pi)$  and it is independent of  $\arg(g_{j,l})$ , since both  $\theta_{j,l}$  and  $\arg(g_{j,l})$  are independent  $U(0, 2\pi)$  RVs. Therefore,  $\hat{\gamma}_{ij}$  is the sum of the products of i.i.d. pairs of complex normal RVs with zero mean and unit variance. To derive the statistical distribution of the real and imaginary parts of  $\hat{\gamma}_{ij}$ , let us express each product term in the sum as

$$\begin{aligned} T_l &= h_{ij,l}\tilde{g}_{j,l} = (a_{ij,l} + j'b_{ij,l})(c_{j,l} + j'd_{j,l}) \\ &= (a_{ij,l}c_{j,l} - b_{ij,l}d_{j,l}) + j'(b_{ij,l}c_{j,l} + a_{ij,l}d_{j,l}), \end{aligned} \quad (41)$$

where  $a_{ij,l}$  and  $b_{ij,l}$  are the real and imaginary components of  $h_{ij,l}$ , respectively, while  $c_{j,l}$  and  $d_{j,l}$  are the real and imaginary components of  $\tilde{g}_{j,l}$ , respectively. It should be noted that  $a_{ij,l}$ ,  $b_{ij,l}$ ,  $c_{j,l}$  and  $d_{j,l}$  are i.i.d. Gaussian RVs with zero mean and variance of 0.5. Each product of two Gaussian RVs can be written as

$$a_{ij,l}c_{j,l} = \frac{1}{4} [(a_{ij,l} + c_{j,l})^2 - (a_{ij,l} - c_{j,l})^2]. \quad (42)$$

Assuming that  $G_1 = a_{ij,l} + c_{j,l}$  and  $G_2 = a_{ij,l} - c_{j,l}$ , the random vector  $[G_1, G_2]^T$  can be written as

$$\begin{bmatrix} G_1 \\ G_2 \end{bmatrix} = \begin{bmatrix} 1 & 1 \\ 1 & -1 \end{bmatrix} \begin{bmatrix} a_{ij,l} \\ c_{j,l} \end{bmatrix} = \mathbf{A} \begin{bmatrix} a_{ij,l} \\ c_{j,l} \end{bmatrix}, \quad (43)$$

where  $\mathbf{A} = \begin{bmatrix} 1 & 1 \\ 1 & -1 \end{bmatrix}$ . The random vector  $[G_1, G_2]^T$  is a Gaussian random vector, since it is a linear transformation of another Gaussian random vector. The covariance matrix of  $[a_{ij,l}, c_{j,l}]^T$  is  $0.5\mathbf{I}_2$ , where  $\mathbf{I}_2$  is the identity matrix of size 2. Hence, the covariance matrix of  $[G_1, G_2]^T$  can be given as [21]

$$\text{cov}([G_1, G_2]^T) = 0.5\mathbf{A}\mathbf{I}_2\mathbf{A}^T = \mathbf{I}_2. \quad (44)$$

Therefore,  $G_1$  and  $G_2$  are uncorrelated RVs, since the covariance matrix of  $[G_1, G_2]^T$  is diagonal. Consequently,  $G_1$

and  $G_2$  are independent since they are jointly Gaussian and uncorrelated RVs.

Similarly, assuming that  $F_1 = b_{ij,l} + d_{j,l}$  and  $F_2 = b_{ij,l} - d_{j,l}$ , the product  $b_{ij,l}d_{j,l}$  can be written as

$$b_{ij,l}d_{j,l} = \frac{1}{4} (F_{1,l}^2 - F_{2,l}^2), \quad (45)$$

where both  $F_1$  and  $F_2$  are independent Gaussian RVs. Hence, the real value of  $\hat{\gamma}_{ij}$  can be expressed as

$$\Re(\hat{\gamma}_{ij}) = \sum_{l=1}^{L_j} \Re(T_l) = \frac{1}{4} \sum_{l=1}^{L_j} [(G_{1,l}^2 + F_{2,l}^2) - (G_{2,l}^2 + F_{1,l}^2)]. \quad (46)$$

The  $l$ th term  $G_{1,l}^2 + F_{2,l}^2$  in (46) can be modeled as an exponential RV since it is the sum of two squared i.i.d. Gaussian RVs. The expected value of such exponential RV can be calculated as

$$\begin{aligned} \mu_{\text{exp}} &= \mathbb{E}(G_{1,l}^2 + F_{2,l}^2) = \text{var}(G_{1,l}) + \text{var}(F_{2,l}) \\ &= \text{var}(a_{ij,l} + c_{j,l}) + \text{var}(b_{ij,l} - d_{j,l}) = 2. \end{aligned} \quad (47)$$

Similarly,  $G_{2,l}^2 + F_{1,l}^2$  is an exponential RV with a mean value of 2. Since an  $L_j$  sum of i.i.d. exponential RVs is modeled as an Erlang RV [21],  $\Re(\hat{\gamma}_{ij})$  in (46) can be modeled as a difference between two i.i.d. Erlang RVs both having a shape parameter of  $L_j$  and a scale parameter of 0.5. Therefore, by using the CF of an Erlang RV [21], the CF of  $\Re(\hat{\gamma}_{ij})$  can be given as in Proposition 1.

## APPENDIX B PROOF OF PROPOSITION 2

Let  $X$  be a RV and  $g(x)$  be a real one-dimensional function. Then, the expected value,  $\mathbb{E}[g(X)]$ , can be calculated using the formula [24]

$$\mathbb{E}[g(x)] = \frac{1}{\pi} \int_0^\infty \Re \{ G(z) \Phi(z) \} dz, \quad (48)$$

where  $G(z)$  is the Fourier transform (FT) of the function  $g(x)$  and  $\Phi(x)_X$  is the CF of the RV,  $X$ . Therefore, applying the above rule to average the conditional BER in (29), the average unconditional BER of  $U_k$  can be calculated as

$$BER_{U_k} = \sum_{q=1}^{N_k} \frac{c_{k,q}}{\pi} \int_0^\infty \Re \left( \mathcal{Q}(z) \Phi_{X_{k,q}} \left( \frac{z}{\sigma_n} \right) \right) dz, \quad (49)$$

where  $\mathcal{Q}(z)$  is the FT of the  $Q$ -function, which can be written as

$$\mathcal{Q}(z) = \mathcal{F}(Q(t)) = \mathcal{F} \left( \int_t^\infty e^{-y^2/2} dy \right), \quad (50)$$

where  $\mathcal{F}(\cdot)$  is the FT operator. Using the integral property of the FT in [25] and getting  $\mathcal{F}(e^{-t^2/2})$  from the FT table,  $\mathcal{Q}(z)$  can be given as

$$\mathcal{Q}(z) = \pi \delta(z) + j' \frac{e^{-z^2/2}}{z}, \quad (51)$$

where  $\delta(\cdot)$  is the Dirac delta function. Substituting  $\mathcal{Q}(z)$  into (49), we can obtain the result of Proposition 2.

## REFERENCES

- [1] M. Elbayoumi, M. Kamel, W. Hamouda, and A. Youssef, "NOMA-assisted machine-type communications in UDN: State-of-the-art and challenges," *IEEE Commun. Surv. Tutor.*, vol. 22, no. 2, pp. 1276–1304, 2020.
- [2] O. Maraqa, A. S. Rajasekaran, S. Al-Ahmadi, H. Yanikomeroglu, and S. M. Sait, "A survey of rate-optimal power domain NOMA with enabling technologies of future wireless networks," *IEEE Commun. Surv. Tutor.*, vol. 22, no. 4, pp. 2192–2235, 2020.
- [3] S. M. R. Islam, N. Avazov, O. A. Dobre, and K.-S. Kwak, "Power-domain non-orthogonal multiple access (NOMA) in 5G systems: Potentials and challenges," *IEEE Commun. Surv. Tutor.*, vol. 19, no. 2, pp. 721–742, 2017.
- [4] H. Yahya, A. Ahmed, E. Alsusa, A. Al-Dweik, and Z. Ding, "Error rate analysis of NOMA: Principles, survey and future directions," *IEEE Open J. Commun. Soc.*, vol. 4, pp. 1682–1727, 2023.
- [5] M. A. ElMossallamy, H. Zhang, L. Song, K. G. Seddik, Z. Han, and G. Y. Li, "Reconfigurable intelligent surfaces for wireless communications: Principles, challenges, and opportunities," *IEEE Trans. Cogn. Commun. Netw.*, vol. 6, no. 3, pp. 990–1002, 2020.
- [6] Y. Liu, X. Liu, X. Mu, T. Hou, J. Xu, M. Di Renzo, and N. Al-Dhahir, "Reconfigurable intelligent surfaces: Principles and opportunities," *IEEE Commun. Surv. Tutor.*, vol. 23, no. 3, pp. 1546–1577, 2021.
- [7] B. Zheng, C. You, W. Mei, and R. Zhang, "A survey on channel estimation and practical passive beamforming design for intelligent reflecting surface aided wireless communications," *IEEE Commun. Surv. Tutor.*, vol. 24, no. 2, pp. 1035–1071, 2022.
- [8] R. Chen, M. Liu, Y. Hui, N. Cheng, and J. Li, "Reconfigurable intelligent surfaces for 6G IoT wireless positioning: A contemporary survey," *IEEE Internet Things J.*, vol. 9, no. 23, pp. 23 570–23 582, 2022.
- [9] Q. Wu, S. Zhang, B. Zheng, C. You, and R. Zhang, "Intelligent reflecting surface-aided wireless communications: A tutorial," *IEEE Trans. Commun.*, vol. 69, no. 5, pp. 3313–3351, 2021.
- [10] Q. Wu and R. Zhang, "Intelligent reflecting surface enhanced wireless network via joint active and passive beamforming," *IEEE Trans. Wireless Commun.*, vol. 18, no. 11, pp. 5394–5409, 2019.
- [11] C. Huang, A. Zappone, G. C. Alexandropoulos, M. Debbah, and C. Yuen, "Reconfigurable intelligent surfaces for energy efficiency in wireless communication," *IEEE Trans. Wireless Commun.*, vol. 18, no. 8, pp. 4157–4170, 2019.
- [12] D. Zhao, H. Lu, Y. Wang, H. Sun, and Y. Gui, "Joint power allocation and user association optimization for IRS-assisted mmwave systems," *IEEE Trans. Wireless Commun.*, vol. 21, no. 1, pp. 577–590, 2022.
- [13] Z. Ding, L. Lv, F. Fang, O. A. Dobre, G. K. Karagiannidis, N. Al-Dhahir, R. Schober, and H. V. Poor, "A state-of-the-art survey on reconfigurable intelligent surface-assisted non-orthogonal multiple access networks," *Proc. IEEE*, vol. 110, no. 9, pp. 1358–1379, 2022.
- [14] Y. Liu, X. Mu, X. Liu, M. Di Renzo, Z. Ding, and R. Schober, "Reconfigurable intelligent surface-aided multi-user networks: Interplay between NOMA and RIS," *IEEE Wireless Commun.*, vol. 29, no. 2, pp. 169–176, 2022.
- [15] B. Tahir, S. Schwarz, and M. Rupp, "Analysis of uplink IRS-assisted NOMA under Nakagami-m fading via moments matching," *IEEE Wireless Commun. Lett.*, vol. 10, no. 3, pp. 624–628, 2021.
- [16] —, "Outage analysis of uplink IRS-assisted NOMA under elements splitting," in *Proc. IEEE VTC*, 2021, pp. 1–5.
- [17] Y. Cheng, K. H. Li, Y. Liu, K. C. Teh, and H. Vincent Poor, "Downlink and uplink intelligent reflecting surface aided networks: NOMA and OMA," *IEEE Trans. Wireless Commun.*, vol. 20, no. 6, pp. 3988–4000, 2021.
- [18] B. Y. D. Rito and K. H. Li, "SER-effective constellation scaling and rotation in STAR-RIS-assisted uplink NOMA," *IEEE Commun. Lett.*, vol. 27, no. 9, pp. 2506–2510, 2023.
- [19] Q. Li, M. El-Hajjar, Y. Sun, I. Hemadeh, A. Shojaiefard, Y. Liu, and L. Hanzo, "Achievable rate analysis of the STAR-RIS-aided NOMA uplink in the face of imperfect CSI and hardware impairments," *IEEE Trans. Commun.*, vol. 71, no. 10, pp. 6100–6114, 2023.
- [20] L. Bariah, S. Muhaidat, P. C. Sofotasios, F. E. Bouanani, O. A. Dobre, and W. Hamouda, "Large intelligent surface-assisted nonorthogonal multiple access for 6G networks: Performance analysis," *IEEE Internet Things J.*, vol. 8, no. 7, pp. 5129–5140, 2021.
- [21] A. Papoulis and U. Pillai, *Probability, Random Variables and Stochastic Processes*, 4th ed. McGraw-Hill, Nov. 2001.
- [22] M. AlaaEldin, E. Alsusa, and K. G. Seddik, "IRS-assisted physical layer network coding over two-way relay fading channels," *IEEE Trans. Veh. Technol.*, vol. 71, no. 8, pp. 8424–8440, 2022.

- [23] H. Yahya, E. Alsusa, and A. Al-Dweik, "Exact BER analysis of NOMA with arbitrary number of users and modulation orders," *IEEE Trans. Commun.*, vol. 69, no. 9, pp. 6330–6344, 2021.
- [24] A. Annamalai, C. Tellambura, and V. Bhargava, "A general method for calculating error probabilities over fading channels," *IEEE Trans. Commun.*, vol. 53, no. 5, pp. 841–852, 2005.
- [25] B. Davies, *Integral Transforms and Their Applications*, 3rd ed. Springer New York, NY, Jan. 2002.